


Enhancement of Acoustic Energy Density in Bulk-Wave-Acoustophoresis Devices Using Side Actuation

Wei Qiu[✉],* Thierry Baasch, and Thomas Laurell[†]

Department of Biomedical Engineering, Lund University, Ole Römers väg 3, Lund 22363, Sweden

 (Received 10 January 2022; revised 21 March 2022; accepted 25 March 2022; published 22 April 2022)

A high acoustic energy density is required in the acoustic resonator to increase the throughput of acoustophoresis devices. In this study, through both experiments and numerical simulations, we find that the energy density in bulk-wave-acoustophoresis devices can be enhanced by actuating the device from the side. Based on qualitative free-flow focusing experiments, side actuation shows clear superiority to bottom actuation under various input powers and flow rates. Quantitative measurements using confocal microparticle image velocimetry confirm an increase by a factor of 4 in energy density using side actuation. Numerical simulations reveal that side actuation leads to significant symmetry breaking, which accounts for strong acoustic fields in the channel, and the device energy-conversion efficiency using side actuation is also higher than that using bottom actuation for different device aspect ratios. Submicrometer particle focusing is performed using an acoustophoresis device with side actuation and more than 90% of 500-nm-diameter particles are focused under a total flow rate of $30 \mu\text{l min}^{-1}$ at an input power of 235 mW, achieved without using a power amplifier.

DOI: [10.1103/PhysRevApplied.17.044043](https://doi.org/10.1103/PhysRevApplied.17.044043)

I. INTRODUCTION

Microscale acoustofluidics, referring to the combination of ultrasound with microfluidics, has become an emerging tool in contemporary biotechnology to separate [1–4], align [5], pattern [6–8], trap [9], concentrate [10–13], and wash [14] suspended cells and microorganisms in a gentle and label-free manner. It typically relies on two physical phenomena, i.e., the acoustic radiation force originating from the wave-particle scattering and acoustic streaming typically arising from the acoustic energy dissipation in viscous fluids. Among all the applications, cell handling and separation using acoustophoresis has reached a level of maturity that has allowed its transfer to industry and made it subject to a growing commercialization [15,16]. One essential challenge for this technique to be able to compete with the standard clinical methods, e.g., centrifugation, is the relatively low throughput, which limits the sample volumes and cell numbers that can be processed in a time unit.

The motion of cells in acoustophoresis devices is typically dominated by the acoustic radiation force due to

their relatively large size and hence the throughput for certain separation tasks is determined by the magnitude of the acoustic radiation force. In the context of nanoparticle manipulation, acoustic streaming is commonly a limiting factor, which counteracts the radiation-force-driven particle focusing inside the microchannel. With the recent techniques to suppress acoustic streaming [17–19], the major challenge for nanoparticle manipulation again turns back to the magnitude of the acoustic radiation force. Considering the acoustic radiation force acting on compressible particles in a one-dimensional plane-wave field, which is often the case in acoustophoresis devices for particle separation, its magnitude is proportional to the particle volume, the acoustic contrast factor, the frequency, and the acoustic energy density of the field [20,21]. For biomedical applications, bioparticles with certain sizes need to be handled in media with good biocompatibility, which usually leads to low acoustic contrast factors and consequently calls for an elevated acoustic radiation force. Frequency is one parameter that can be tuned and the increase of the acoustic radiation force by increasing the frequency has been demonstrated [22]. For a resonant cavity operating at its fundamental resonance mode, however, the increase of the frequency results in the decrease of the cavity size, which reduces the sample volumes that can be processed in a time unit and hence limits the device throughput. The last parameter to increase the acoustic radiation force, and hence to improve the throughput of acoustophoresis devices, is the acoustic energy density inside the microchannel, which scales linearly with the

*wei.qiu@bme.lth.se

†thomas.laurell@bme.lth.se

Published by the American Physical Society under the terms of the [Creative Commons Attribution 4.0 International](https://creativecommons.org/licenses/by/4.0/) license. Further distribution of this work must maintain attribution to the author(s) and the published article's title, journal citation, and DOI. Funded by [Bibsam](https://www.bibsam.se/).

acoustic radiation force acting on suspended particles. Since the infancy of microscale acoustofluidics in the early 2000s, there have been surprisingly few research efforts working on the enhancement of the device energy density [23–25] and the typical way used in the community to achieve a high energy density is to apply a high electric power to piezoelectric transducers with power amplifiers. This method is far from ideal, because a large proportion of the input power will be converted to loss when the energy-conversion efficiency from electric energy to acoustic energy is low. The energy loss will result in a considerable temperature rise, which may harm the biological samples to be processed and affect the chip performance due to the shift of the resonance frequency. In addition, piezoelectric materials work in their nonlinear regime under a high electric field strength, described by the well-known hysteresis loops of piezoelectric materials [26]; thus an increase in the acoustic energy inside the microchannel cannot always be guaranteed by increasing the input power.

Bulk-wave-acoustophoresis devices typically generate standing-wave fields either in the transverse direction (along the channel width) or in the vertical direction (along the channel height). It is easier to achieve high throughput in the latter, the so-called planar resonant devices, compared to the former due to the large channel width that they possess [27–30]. However, the difficulty in generating uniform sound fields along the full channel width in planar devices leads to a high contamination rate when performing separation tasks, which hinders their usage in practical applications.

When designing acoustophoretic resonators with sound fields in the transverse direction, it seems most natural to actuate the system in the same direction as the standing-wave field, as performed in early work by Yasuda *et al.* using a millimeter-sized device [31]. Here, we call this

type of actuation *side actuation*, since the piezoelectric transducer is mounted on the side of the device, as illustrated in Fig. 1(b). However, when the resonators are implemented at microchip level, the piezoelectric transducers are commonly mounted on the bottom of the microchip in bulk acoustophoresis devices [32–35], called *bottom actuation* and shown in Fig. 1(c). This configuration operates the transducers under a dominant thickness mode with a mixture of high-order transverse modes and provides the benefits of easy mounting of the transducer as well as a larger area for mechanical coupling to the bottom of the chip than that on the side. Acoustophoresis devices using transverse sound fields offer easy optical access to the acoustophoretic motion of particles or cells, but the channel volumes are smaller than those of the planar devices and hence a high acoustic energy density in the channel is critical for achieving high throughput. From the viewpoint of the coupling efficiency of vibration modes, recent work has demonstrated that the energy density obtained in the microchannel can be improved by breaking the actuation symmetry [24,25]. This idea is interesting; however, it requires two channels of electric signals with an optimal phase difference and the comparison of the coupling efficiency between different actuation modes is not clearly conducted. In this study, through comprehensive experiments and numerical simulations, we show that the energy density of acoustophoresis devices, and thus the acoustic radiation force exerted on particles, can be enhanced by a factor of 4 under the same input power simply by mounting the piezoelectric transducer at the side of the microchip, which indicates a significantly improved energy-conversion efficiency of the device. The physical mechanism regarding the improvement of energy density using side actuation is uncovered and discussed. We further demonstrate the focusing of 500-nm-diameter particles with side actuation and a recovery rate higher than

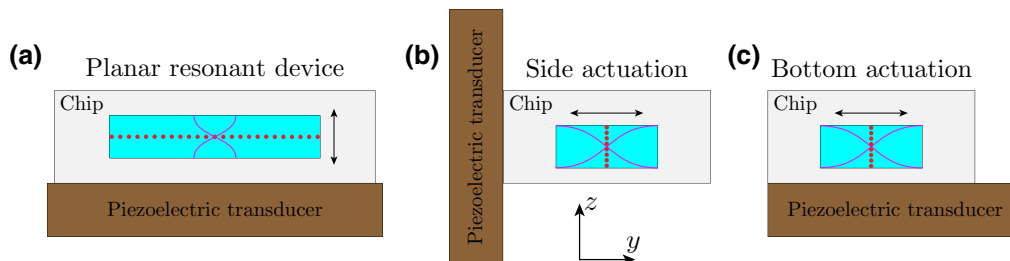


FIG. 1. A sketch of (a) the planar resonant device and the devices with transverse sound fields driven by (b) side and (c) bottom actuation in cross-section view. In the planar device, a half-wave standing-wave field (magenta) is created in the vertical direction in the channel (blue) and the particles (red) above the critical particle size are levitated to the channel midheight. In the devices with transverse sound fields, a half-wave standing-wave field is generated in the transverse direction, irrespective of the position of the piezoelectric transducer (brown), and the particles above the critical particle size are focused to the center of the channel width. The black arrows indicate the directions of fluid oscillations and hence the orientation of the sound fields. The channel dimensions are enlarged compared to the dimensions in actual devices for better visibility.

90% is obtained under a total flow rate of $30 \mu\text{l min}^{-1}$ at an input power of 235 mW, achieved without using a power amplifier.

II. MATERIALS AND EXPERIMENTAL METHODS

A. Materials and experimental setup

Nine glass chips with the same outer and channel dimensions are used to compare the chip performance under different actuation modes. The chips have an outer dimension of $70 \times 3 \times 1.1 \text{ mm}^3$ and an isotropically etched channel dimension of length $L = 45 \text{ mm}$, width (at its top) $W = 0.403 \text{ mm}$, and height $H = 0.133 \text{ mm}$. Each chip consists of two inlets and two outlets. Only the center inlet and outlet are used (the side inlet and outlet are blocked by dead ends) in the experiments for evaluating chip performance, while all the inlets and outlets are used in submicrometer particle-focusing experiments. Lengths of silicone tubing (outer diameter 3 mm, inner diameter 1 mm, and length 9 mm) are glued to the chip inlets and outlets using a silicone glue. Lead zirconate titanate (PZT) transducers (Pz26, Ferroperm Piezoceramics, Kvistgaard, Denmark) with a length of 25 mm and a thickness of 1 mm are glued either underneath or to the chip sidewall using cyanoacrylate glue (Loctite Super Glue, Henkel Norden AB, Stockholm, Sweden), which forms a total of three configurations under test (see Fig. 2). Two configurations, one actuated from the bottom and one actuated from the side, use the PZT transducers with the same width (5 mm). When the PZT transducer is mounted at the side, a large fraction of the transducer area is not in contact with the chip. In the third configuration, therefore, a PZT transducer with a smaller width (2 mm) is used, which leads to a similar ratio of the transducer area to the contact area in bottom and side actuation. Three chips are tested using each configuration, to improve the statistics.

The PZT transducers are driven by a function generator (33220, Agilent Technologies, Inc., Santa Clara, California), and the waveforms of the applied voltages to the transducers and the resulting currents are monitored by a PicoScope (5244D, Pico Technology, Cambridgeshire, United Kingdom). The input power to the PZT transducer is measured using voltage and current probes and then calculated by time averaging the product of the voltage and current over multiple cycles. Fluorescent green polystyrene beads with a nominal diameter of $4.9 \mu\text{m}$ (G0500B, Fluoro-Max, Thermo Fisher Scientific, Waltham, Massachusetts) are used to characterize the chip performance. The fluorescent particles are mixed in Milli-Q water and the volume fraction of the suspension is 0.1%, which is far below the limit where hydrodynamic or acoustic particle-particle interactions will occur [37].

All the experiments are performed using a confocal microscope (Eclipse Ti2, Nikon, Tokyo, Japan) equipped

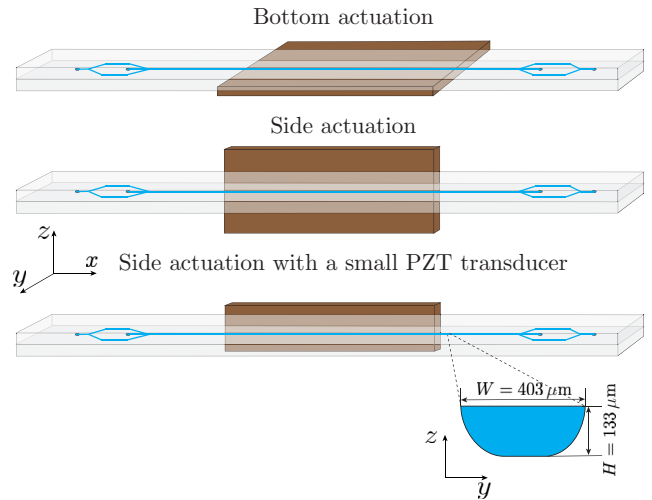


FIG. 2. A sketch of the acoustophoresis glass chips (light gray) with a dimension of $70 \times 3 \times 1.1 \text{ mm}^3$. The long straight microchannel (light blue) has dimensions of 45×0.403 (at its top) $\times 0.133 \text{ mm}^3$. The PZT transducer (brown) is mounted either at the bottom or at the side of the chip. The PZT transducers in the top two configurations have dimensions of $25 \times 5 \times 1 \text{ mm}^3$, while the PZT transducer in the lower configuration has dimensions of $25 \times 2 \times 1 \text{ mm}^3$. The inset shows the channel cross section. A photograph of the actual devices can be found in the Supplemental Material [36].

with a spinning disk unit (X-Light V3, Crest, Rome, Italy) and a CMOS camera (Prime 95B, Teledyne Photometrics, Tucson, Arizona). Blue fluorescent excitation light is illuminated from a laser diode with a peak wavelength of 488 nm, and a standard fluorescence filter cube is used with an excitation pass band from 475 to 495 nm and an emission pass band from 510 to 531 nm. An objective lens with $10\times$ magnification and 0.3 numerical aperture is used and this configuration provides a field of view of $1.83 \times 1.83 \text{ mm}^2$ and an optical slice thickness of $5.7 \mu\text{m}$.

B. Free-flow focusing experiments

To compare the chip performance under different actuation methods, the solution with fluorescent polystyrene particles is injected and flowed through the channel while the sound field is turned on. For $4.9\text{-}\mu\text{m}$ -diameter polystyrene particles in water at a frequency of around 2 MHz, their motion is dominated by the acoustic radiation force and the contribution from the acoustic streaming can be neglected [38–40]. The particles are injected in the channel with a uniform distribution near the center inlet using a syringe pump (neMESYS, Cetoni GmbH, Korbussen, Germany) with flow rates controlled by a computer interface, and migrated toward the pressure nodal plane due to the radiation force, forming a narrow band before exiting the outlet. The particle bandwidth at the outlet indicates the averaged acoustic radiation force and hence the

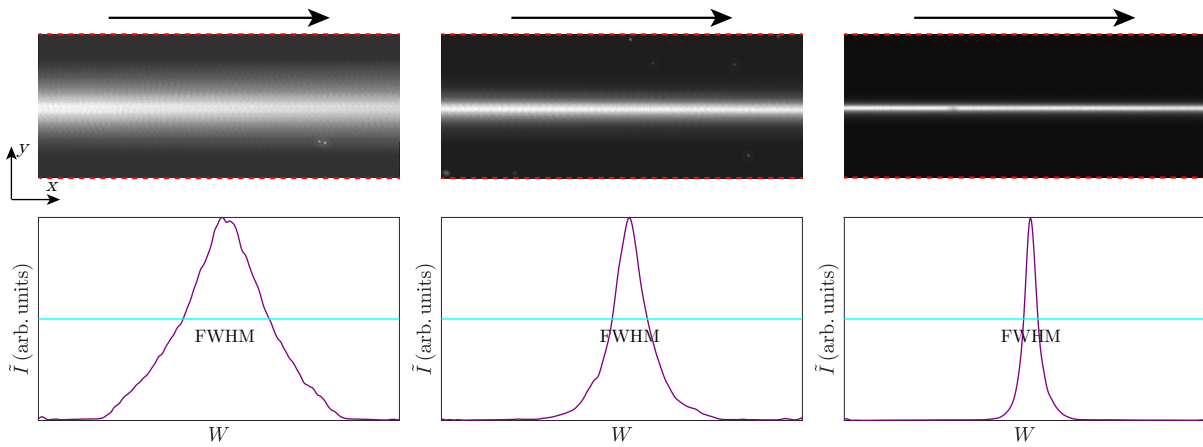


FIG. 3. An illustration of free-flow focusing measurements for qualitative comparison of chip performance. The top row shows the particle-focusing band under three energy densities averaged over 100 frames, taken in a 0.92-mm-long section at the end of the straight channel. The flow direction is from the left to the right, indicated by the arrows. The channel sidewalls are indicated by red dashed lines. The normalized intensity profile \tilde{I} in each case (purple) is plotted by averaging the intensity values along the channel length (x) direction, as shown in the lower row. The full width at half maximum (FWHM) is determined by the width of the intersection between \tilde{I} and $\tilde{I} = \tilde{I}_{\max}/2$ (cyan).

energy density E_{ac} along the whole channel [41]. Here, we define a dimensionless parameter, i.e., the normalized particle bandwidth \tilde{B} , which is the ratio of the full width at half maximum (FWHM) of the fluorescence intensity profile to the channel width W , as shown in Fig. 3. A small \tilde{B} indicates a high E_{ac} in the channel when the flow rate is constant. This method is a qualitative yet rapid approach to find the resonance frequency and examine the chip performance. The measurements are conducted in the end section of the straight channel with a length of 0.92 mm and the focal plane is placed at channel midheight. A total of 100 frames are recorded at a frame rate of 100 frames/s and an exposure time of 10 ms. All the frames are then stacked and averaged and the final intensity profile is obtained by averaging the intensity along the length direction.

When PZT transducers are mounted at different positions or have different dimensions, the resonators reveal different frequency responses and the resonance frequency of each chip therefore varies slightly. We first find the resonance frequency of each chip using the above-mentioned free-flow focusing method by sweeping the frequency under constant applied voltages and an example of this measurement is given in Fig. 4. It turns out that the resonance frequency of each chip does not change when the applied voltage varies within the voltage range used in this experiment (1.99 V_{pp} to 10.30 V_{pp}), which is expected for linear systems. To compare the performance of the different chip configurations, the input powers to the PZT transducers P_{in} and the flow rates Q are fixed. Four different P_{in} , i.e., 12.5 mW, 25 mW, 50 mW, and 100 mW, are applied and the corresponding flow rates at each P_{in} are 175 $\mu\text{l min}^{-1}$, 350 $\mu\text{l min}^{-1}$, 725 $\mu\text{l min}^{-1}$, and

1050 $\mu\text{l min}^{-1}$, respectively. If the flow rate is too low, the particle-focusing bands of the two chips with different E_{ac} may both be saturated (all the particles are focused to the pressure nodal plane); hence the difference in E_{ac} cannot be distinguished. Thus, the flow rate at each P_{in} is determined to ensure that the particle-focusing band for the chip with the highest E_{ac} is not saturated. The flow rates are monitored using a flow sensor (SLI-1000, Sensirion AG, Stäfa, Switzerland) throughout the experiments. The driving conditions for all the nine chips tested in free-flow focusing experiments using different actuation methods are summarized in the Supplemental Material [36].

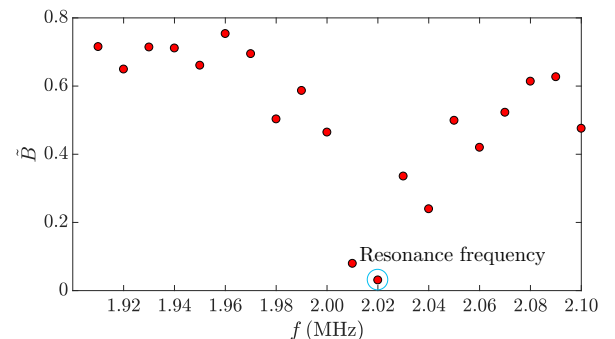


FIG. 4. An example of finding the resonance frequency using free-flow focusing measurements. The normalized particle bandwidth \tilde{B} is measured in a frequency range from 1.91 to 2.10 MHz with an interval of 0.01 MHz under a constant applied voltage. The resonance frequency is determined by the smallest \tilde{B} , indicated by a cyan circle.

C. Confocal micro-PIV measurements

To quantify the energy density E_{ac} under different actuation methods, confocal microparticle-image-velocimetry (PIV) measurements are conducted for the chips actuated from the bottom and from the side with a small PZT transducer under the stop-flow condition. This measurement is based on the balance of the acoustic radiation force \mathbf{F}_{rad} and the Stokes drag force \mathbf{F}_{drag} . Extended from the theory of Yosioka and Kawasima and Gor'kov [20,21], for the case of a half-wavelength standing-wave field in the channel width (y) direction \mathbf{e}_y , the analytical solution for the time-averaged \mathbf{F}_{rad} on a single freely suspended spherical particle of radius a , density ρ_p , and compressibility κ_p in a viscous fluid of density ρ_f , compressibility κ_f , and viscosity η_0 can be expressed as [42]

$$\mathbf{F}_{rad}(y) = 4\pi a^3 k_y E_{ac} \Phi(\tilde{\kappa}, \tilde{\rho}, \tilde{\delta}) \sin(2k_y y) \mathbf{e}_y, \quad (1a)$$

$$\Phi(\tilde{\kappa}, \tilde{\rho}, \tilde{\delta}) = \frac{1}{3} f_0(\tilde{\kappa}) + \frac{1}{2} \text{Re}[f_1(\tilde{\rho}, \tilde{\delta})], \quad (1b)$$

here k_y and Φ are the wave number and acoustic contrast factor, respectively. The monopole and dipole scattering coefficients f_0 and f_1 are given by

$$f_0(\tilde{\kappa}) = 1 - \tilde{\kappa}, \quad f_1(\tilde{\rho}, \tilde{\delta}) = \frac{2[1 - \Gamma(\tilde{\delta})](\tilde{\rho} - 1)}{2\tilde{\rho} + 1 - 3\Gamma(\tilde{\delta})}, \quad (1c)$$

where $\Gamma(\tilde{\delta}) = -3/2[1 + i(1 + \tilde{\delta})]\tilde{\delta}$, with $\tilde{\kappa} = \kappa_p/\kappa_f$, $\tilde{\rho} = \rho_p/\rho_f$, and $\tilde{\delta} = \delta/a$ ($\delta = \sqrt{2\eta_0/(\rho_f\omega)}$ is the thickness of the viscous boundary layer). The time-averaged \mathbf{F}_{drag} on a spherical particle moving with a velocity \mathbf{u} in a fluid neglecting the acoustic streaming is expressed as

$$\mathbf{F}_{drag} = 6\pi\eta_0 a \mathbf{u}. \quad (2)$$

The ratio of the particle displacement under acceleration to a is small [43]; hence the particle acceleration is negligible and the measured \mathbf{u} is always the terminal velocity under the equilibrium condition $\mathbf{F}_{rad} = \mathbf{F}_{drag}$. By measuring the focusing velocity of 4.9- μm -diameter polystyrene particles in water using micro-PIV, E_{ac} can be obtained. It should be noted that the streaming contribution to the particle-focusing velocity is sufficiently small for this size of polystyrene particles in water at 2 MHz [38–40]; thus it is neglected in our calculation. However, this theory does not apply and will lead to considerable error when particles migrate near the top or bottom wall, due to the acoustic and hydrodynamic particle-wall interactions [44–47]. This problem is automatically solved when confocal microscopy is used. By placing the focal plane at the channel midheight, the optical slice with a thickness

of 5.7 μm is far from the channel top and bottom; hence the particles moving near the top and bottom walls cannot be captured. The confocal micro-PIV therefore provides measurements with higher accuracy compared to the PIV measurements performed using compound microscopes [48].

The measurements are conducted in the channel region covered by the PZT transducer, because the sound field outside this region is very weak. To cover the 25-mm-long channel region, the measurements are divided into 14 sections. For each section, 10–25 repetitions are performed to improve the accuracy of the measurement, resulting in 100–700 frames recorded under a frame rate of 140 frames/s and an exposure time of 7 ms. The recorded frames correspond to a time period ranging from 0.007 s to 0.5 s after the PZT transducer is switched on, which guarantees that no significant particle depletion occurs in the last frame of each PIV analysis. Due to the limitation of the camera frame rate, the micro-PIV measurements are only performed under 12.5 mW input power, above which the particle images become distorted due to the fast particle motion. A MATLAB-based open-source PIV algorithm, PIVlab, is used to process the data [49].

D. Submicrometer particle focusing

One of the chips using side actuation with a small PZT transducer is used for focusing submicrometer particles. When the particle size is below the critical size (about 2 μm in diameter in our system), the streaming-induced drag force dominates over the acoustic radiation force and prevents the particles from being focused. This problem can be solved by using a medium with an inhomogeneous density and compressibility, which significantly suppresses the acoustic streaming in the channel [17,18]. The inhomogeneous medium is created by laminating phosphate-buffered saline (PBS) at the side of the channel and 25-wt% Percoll in PBS at the center, resulting in a density difference of 2.89% and a compressibility difference of 2.44% at 25 °C. The submicrometer particles with a nominal diameter of 500 nm (G500, Fluoro-Max, Thermo Fisher Scientific, Waltham, Massachusetts) are mixed in PBS with a solid concentration of 0.003% and infused to the channel as the side stream, as sketched in Fig. 5. The solutions are injected to the channel with a total flow rate of 30 $\mu\text{l min}^{-1}$ (13 $\mu\text{l min}^{-1}$ for the side stream and 17 $\mu\text{l min}^{-1}$ for the center stream) using a syringe pump (neMESYS, Cetoni GmbH, Korbussen, Germany). Five different powers, i.e., 25 mW, 75 mW, 125 mW, 175 mW, and 235 mW, are applied to the PZT transducer, which are all realized without using a power amplifier. The particle focusing is run for 10 min under each input power and the device is cooled using compressed air throughout the experiments. The particles collected from the side and center outlets are counted using Nanoparticle Tracking Analysis (NanoSight LM10,

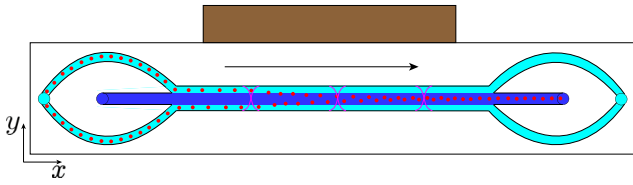


FIG. 5. An illustration of the submicrometer particle focusing in a streaming-suppressed medium using side actuation. The PZT transducer (brown) is mounted at the side of the chip to induce a half-wave standing-wave field (magenta). Two fluids are laminated to the channel (the flow direction is indicated by the arrow), with the fluid of low acoustic impedance (light blue) at the side and the fluid of high acoustic impedance (blue) in the center. The induced acoustic body force stabilizes the fluid configuration [50] and suppresses the acoustic streaming [17,18]. The submicrometer particles (red) are infused to the channel through the side stream and are focused to the center by the acoustic radiation force without the disturbance of acoustic streaming.

Malvern Panalytical, Malvern, United Kingdom). Each focusing experiment is repeated three times to validate the accuracy of the measurement.

III. NUMERICAL MODEL

The numerical simulations are performed using the finite-element (FE) software COMSOL MULTIPHYSICS 5.5 [51] and the model details are presented in the following.

A. Model system and computational domain

The 2D model of the acoustophoresis device consists of a water channel placed at the center of a glass domain and driven by a PZT transducer (Pz26) that is attached via a 5- μm -thick glue layer. We introduce four geometrically different FE setups, which are distinguished by the placement of the PZT transducer. The transducer is either

omitted in the model or attached at the bottom or the side of the device. The setups are denoted by no piezo (*np*), bottom actuation with piezo (*bap*), side actuation with piezo (*sap*), and side actuation with small piezo (*sasp*), respectively [see Figs. 6(a)–6(d)]. The dimensions of the chip, the channel, and the PZT transducer in the numerical simulations match the dimensions in the experiments. Numerical models are also built for the same devices with rectangular channel cross sections ($W = 375 \mu\text{m}$ and $H = 150 \mu\text{m}$) [36], which is also a common channel geometry in acoustofluidic devices. In the *bap* model, the transducer has an overhang to the right side of the device and a small offset of $200 \mu\text{m}$ to the left, as shown in Fig. 6(b). All relevant material properties are listed in Table I.

The fluid domain is modeled including viscous but not thermal effects. The glass and transducer domains are considered as linear elastic solids and the piezoelectric effect is included in the domain of the PZT transducer. We assume the chip to be acoustically isolated and thus we neglect any acoustic radiation away from the chip. Both the losses due to internal friction inside the glass as well as the losses due to viscous effects contribute to the damping in the *np* models. In the models including the PZT transducer (*bap*, *sap*, and *sasp*), an additional glue layer between the transducer and the device is included and the losses inside the glue layer and the transducer are additional damping mechanisms.

B. Mesh

The geometry is discretized mostly by a quadratic mesh. A triangular mesh is applied close to the water channel to properly discretize the curvature of the water channel. An additional boundary layer mesh is introduced at the channel walls inside the water domain to discretize the high velocity gradients due to the viscous boundary layer. The size of the mesh is determined by a mesh-convergence

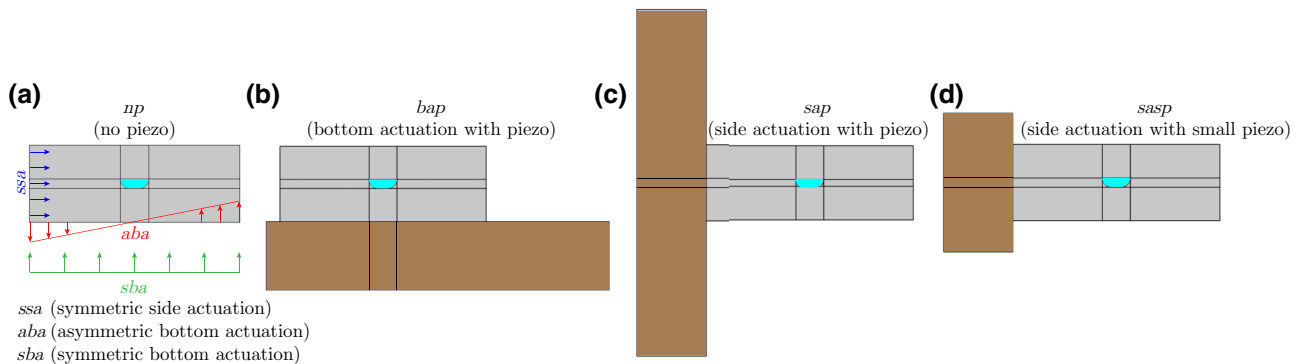


FIG. 6. An illustration of the two-dimensional (2D) models used in the numerical simulations. The glass, PZT transducer, and water domains are indicated by gray, brown, and cyan, respectively. (a) The model without a PZT transducer (*np*). Three different actuation methods—symmetric (*sba*) and asymmetric (*aba*) bottom actuation, and symmetric side actuation (*ssa*)—are indicated by green, red, and blue arrows, respectively. (b) Bottom actuation with a PZT transducer (*bap*). (c) Side actuation with a PZT transducer (*sap*). (d) Side actuation with a small PZT transducer (*sasp*).

TABLE I. The model parameters. The parameters are given at room temperature. The properties of Pz26 are taken from Ferroperm Piezoceramics [52] and are not listed here.

Water		
Density	1000	kgm^{-3}
Speed of sound	1481	ms^{-1}
Dynamic viscosity	1	mPa s
Bulk viscosity	2.85	mPa s
Pyrex glass [53]		
Density	2240	kgm^{-3}
Poisson's ratio	0.245	
Young's modulus	$60(1 + i/2420)$	GPa
Glue layer		
Thickness	5	μm
First Lamé parameter	$4.82(1 + i/10)$	GPa
Second Lamé parameter	$2.06(1 + i/10)$	GPa

study for the symmetric side actuation without the PZT transducer (*ssa*) and the bottom actuation with a PZT transducer (*bap*) models, as shown in Fig. 7. The quality of the mesh is described by the degree of freedom of the tested mesh divided by the degree of freedom of the most accurate mesh that is used with the respective model. In that way, a low or high performance number indicates a coarse or fine mesh. It is worth noting that the maximum degree of freedom is not the same for the models with and without a PZT transducer.

C. Actuation methods

A total of three different actuation methods are applied in the *np* model, as illustrated in Fig. 6(a). In the symmetric bottom actuation (*sba*), the complete bottom of the glass is harmonically displaced by 1 nm in phase at the excitation

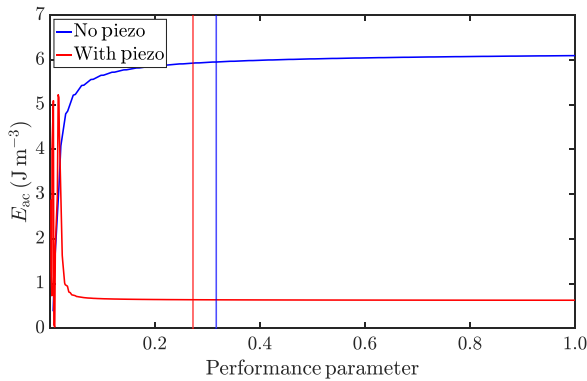


FIG. 7. The results of the mesh study are shown for both setups with (*bap*) and without (*ssa*) a piezoelectric transducer. The meshes used in this study are indicated by the two vertical lines. The performance parameter is defined as the ratio of the degree of freedom of the current to the most precise mesh.

frequency. In the asymmetric bottom actuation (*aba*), the displacement amplitude varies linearly along the wall from the positive to the negative maximal displacement of 1 nm, thus breaking the symmetry. Only one side of the device is harmonically excited at 1 nm in the symmetric side actuation (*ssa*) model. In the three models with PZT transducers (*bap*, *sap*, and *sasp*), a voltage of 5 V_{pp} is applied to the transducer. The average acoustic energy density inside the water channel is evaluated over a frequency range from 1.75 MHz to 2.1 MHz for all the different settings.

IV. RESULTS AND DISCUSSION

A. Comparison between different actuation methods

The chip performance using different actuation methods is compared qualitatively by free-flow focusing measurements, as shown in Fig. 8. It is found that the normalized particle bandwidth \tilde{B} under side actuation is smaller than that under bottom actuation in all cases when the experimental conditions are the same, indicating that a higher energy density E_{ac} is achieved using side actuation. Among the two configurations with side actuation, the chips using smaller PZT transducers show clear superiority to those using larger transducers. The input power P_{in} to all the three chips actuated by the small PZT transducers from the side can reach 200 mW without using amplifiers, under which 4.9- μm -diameter polystyrene particles can be completely focused ($\tilde{B} < 0.05$) at a flow rate of 2 ml min^{-1} . Such a high throughput has not been reported when the device is only driven by a function generator [29].

The E_{ac} values under bottom actuation and side actuation with a small PZT transducer are measured using confocal micro-PIV under $P_{in} = 12.5$ mW (see Fig. 9). Both the averaged E_{ac} for the whole 25-mm-long actuation region and the local E_{ac} for each 240- μm -long section are calculated and the results confirm that side actuation leads to a higher E_{ac} . The averaged E_{ac} among the three chips using side actuation with small PZT transducers shows an increase by a factor of 4 compared to the chips using bottom actuation and the maximum local E_{ac} is also higher with side actuation. One distinct difference between the two actuation modes is that the hot spots (the regions with relatively high local E_{ac}) appear in a considerably wider region inside the channel with side actuation, while they are confined in small regions with bottom actuation, as previously reported [48].

B. Simulation results

To understand why side actuation leads to higher E_{ac} compared to bottom actuation, we first simulate three ideal actuation methods excluding the PZT transducer in the model, i.e., symmetric (*sba*) and asymmetric (*aba*) bottom actuation, and symmetric side actuation (*ssa*), as illustrated in Fig. 6(a). In the case of bottom actuation, *sba* results in

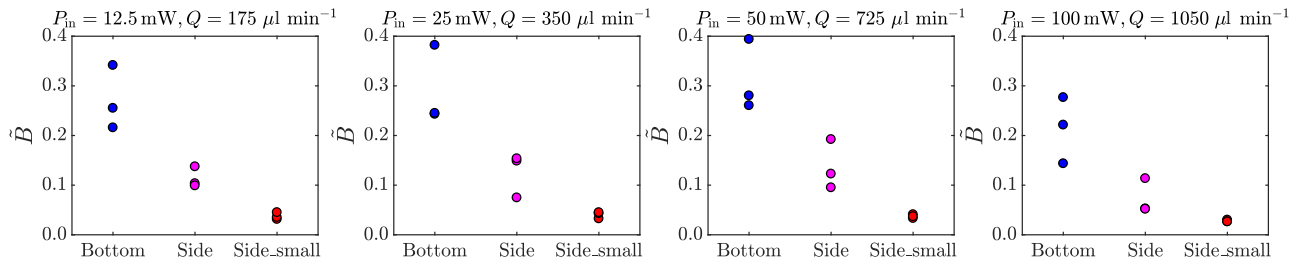


FIG. 8. A qualitative comparison of the chip performance using bottom (blue) and side (pink) actuation, and side actuation with a small PZT transducer (red) under four different conditions, indicated by the normalized particle-focusing bandwidth \bar{B} . The three points using the same color represent the three tested devices under each actuation mode.

a weak acoustic field in the channel [Fig. 10(a)], while a strong acoustic field is obtained by *aba* [Fig. 10(b)]. The two channel sidewalls move in phase horizontally using *aba*, which is the key to producing strong transverse sound fields, as predicted in Ref. [39]. The vibration modes of the chip and the channel walls produced by *ssa* [Fig. 10(c)] are different from that produced by *aba*, where two channel sidewalls still move in phase horizontally but with the channel expanded on one side and contracted on the other side. Both *aba* and *ssa* lead to strong sound fields and high E_{ac} , as shown in Fig. 11(a). We also confirm that *sba*, *aba*, and *ssa* induce qualitatively the same vibration modes of the channel walls with a rectangular cross section (see the Supplemental Material [36]). It has been reported that a strong acoustic field inside the channel requires symmetry breaking [24,54], which can be realized by not only *aba* but also *ssa*. In a more realistic model with the PZT transducer, symmetry is already broken to some extent with bottom actuation (*bap*) when the PZT transducer is mounted with an offset, as shown in Fig. 10(d). The excited vibration mode of the channel walls is similar to that excited by *ssa*. However, the wall vibration and hence the symmetry breaking are not as significant as that in the ideal case, resulting in a relatively weak sound field. Significant symmetry breaking of the device using bottom actuation requires either geometric asymmetry [25] or antisymmetric driving of the PZT transducer [24], which tends to induce a vibration mode of the channel walls similar to that obtained in the ideal *aba*. On the other hand, we find that strong symmetry breaking can also be achieved using side actuation, which is proven by the vibration mode shown in the side actuation models with the PZT transducer (*sap* and *sasp*), as revealed in Figs. 10(e) and 10(f), leading to stronger sound fields and higher E_{ac} in the channel compared to those using *bap*, as shown in Fig. 11(b). All three actuation methods (*bap*, *sap*, and *sasp*) lead to similar vibration modes of the channel walls; nevertheless, the wall displacement is amplified more with side actuation, resulting in a higher E_{ac} than that generated by *bap*. The vibration modes of the channel walls with rectangular channel cross sections are nearly qualitatively

identical to the modes excited with bowl-shaped channel cross sections [36], indicating that the symmetry breaking induced by side actuation can be achieved in both channel geometries. Animations of all six vibration modes shown in Fig. 10 can be found in the Supplemental Material [36].

When finding the resonance frequency of acoustophoresis devices, the applied voltage to the PZT transducer is typically fixed during the frequency sweep and then the frequency at which E_{ac} is the highest is sought, as performed in both experiments (Fig. 4) and simulation [Fig. 11(b)]. This method of frequency seeking corresponds to finding the resonance frequency of an electrical system by applying a constant voltage or of a mechanical system by applying a constant force. On the other hand, it is also possible to determine the driving frequency from the point of view of energy-conversion efficiency. Here, we define a dimensionless efficiency parameter $\hat{\eta}_{eff} = \omega E_{ac} V_l / P_{in}$, where ω and V_l are the angular frequency and the unit volume. This parameter describes the ratio of stored acoustic energy in the channel to the energy loss of the system per cycle, which indicates the energy-conversion efficiency from electric power to the PZT transducer to the acoustic power in the channel. The dependence of $\hat{\eta}_{eff}$ on the frequency reveals that side actuation also results in a higher energy-conversion efficiency compared to bottom actuation, as shown in Fig. 11(c), which is in good agreement with the experimental results. In addition, the $\hat{\eta}_{eff}$ using *sasp* is higher than that using *sap*, which is also observed in experiments (Fig. 8). This fact intuitively indicates that only a small amount of the total vibrational energy is coupled to the chip when the device side area is much smaller than the transducer area. Further investigations are needed to fully understand the reasons that cause the difference in actuation performance when the transducer dimensions vary. The same trend regarding $\hat{\eta}_{eff}$ is also found in the devices with rectangular channel cross sections [36]. It is worth noting that the frequency where the highest $\hat{\eta}_{eff}$ is achieved does not match the system resonance frequency perfectly. In this work, the driving frequency selected for each chip is the system resonance frequency found by sweeping the frequency under a

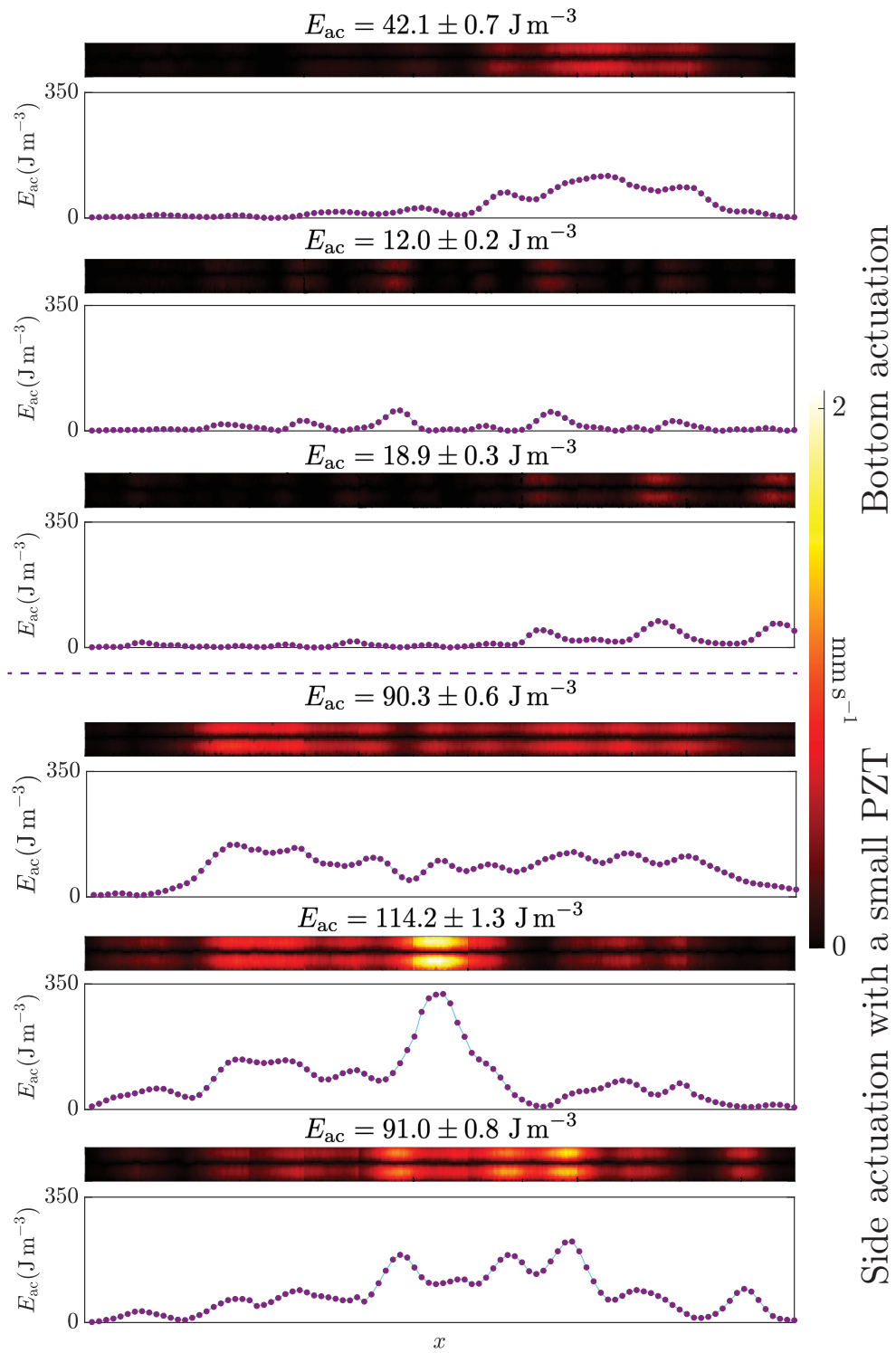


FIG. 9. Micro-PIV measurements of E_{ac} under bottom actuation and side actuation using a small PZT transducer with $P_{in} = 12.5$ mW in a 25-mm-long region where the PZT transducer is located. The color plot shows the particle-focusing velocity from 0 (black) to 2.07 mms^{-1} (white). The E_{ac} value on top of each color plot is the averaged E_{ac} for the whole measured region, while the local E_{ac} along every $240 \mu\text{m}$ -long section is plotted below each color plot in a range between 0 and 350 J m^{-3} . The width dimension is expanded by a factor of 3 for better visibility.

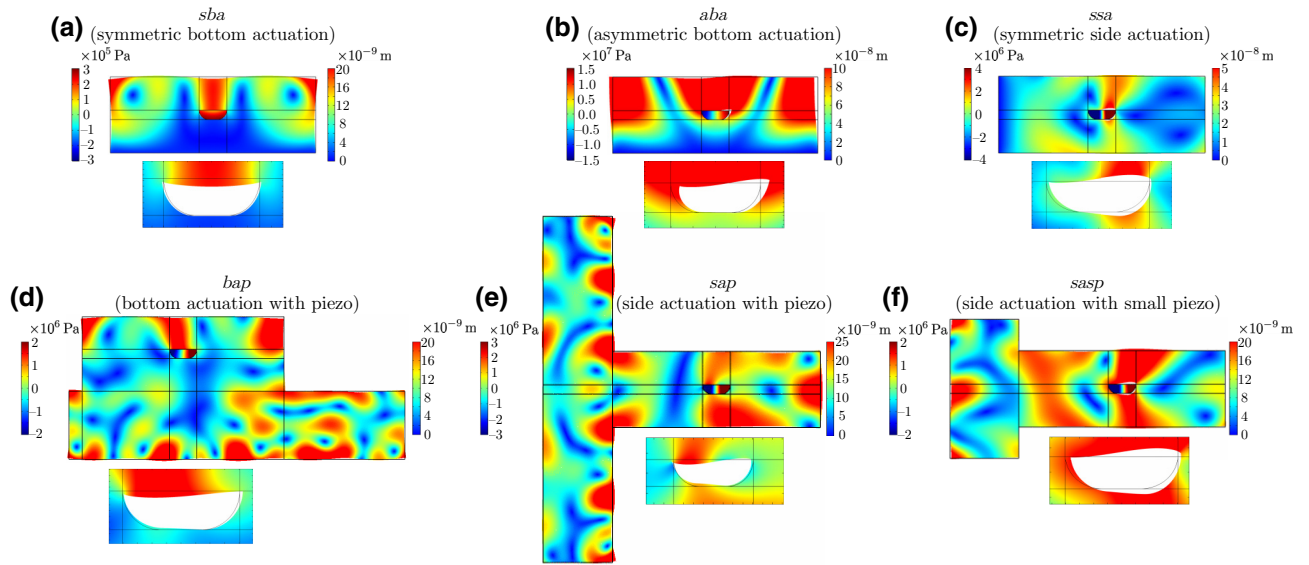


FIG. 10. Vibration modes and induced sound fields inside the channels using (a) *sba*, (b) *aba*, and (c) *ssa* obtained by the ideal models without a PZT transducer, and using (d) *bap*, (e) *sap*, and (f) *sasp* obtained by the models with PZT transducers. The channel region is enlarged and placed under each plot of the vibration mode of the whole device to illustrate the vibration mode of the channel walls. The color bar on the left side of each plot indicates the color scale of the pressure field in the channel, while the color bar on the right side indicates the color scale of the displacement in the solid.

constant applied voltage. This is because at the resonance frequency a certain P_{in} can be achieved with a lower voltage compared to that at other frequencies off resonance, which is important in terms of device driving. We also would like to emphasize here that when comparing the performance of several devices, fixing the applied voltage to the PZT transducer, as shown in Fig. 11(b), does not lead to a fair comparison, though it is widely used in the community. This is because the electrical impedance of different devices varies, particularly when they are driven under distinct modes. This fact inherently results in different P_{in} to the devices when applying a constant voltage. Therefore, in this study, experimentally the P_{in} to

different chips is matched at their resonance frequencies and numerically $\hat{\eta}_{eff}$ is introduced when comparing chip performance, where P_{in} is normalized.

We also conduct a parametric study in numerical simulation to investigate the effect of the device aspect ratio $\alpha = H/W$ on $\hat{\eta}_{eff}$ using *bap* and *sap*. It is found for the α range under investigation ($0.12 < \alpha < 1$), including the α used in our experiments ($\alpha = 0.37$), that the $\hat{\eta}_{eff}$ is always higher with side actuation (see Fig. 12). Furthermore, it is easier to obtain high $\hat{\eta}_{eff}$ using side actuation compared to bottom actuation, as indicated by the larger area of high $\hat{\eta}_{eff}$ in Fig. 12. The simulation results obtained from the models with rectangular channel cross sections lead to the

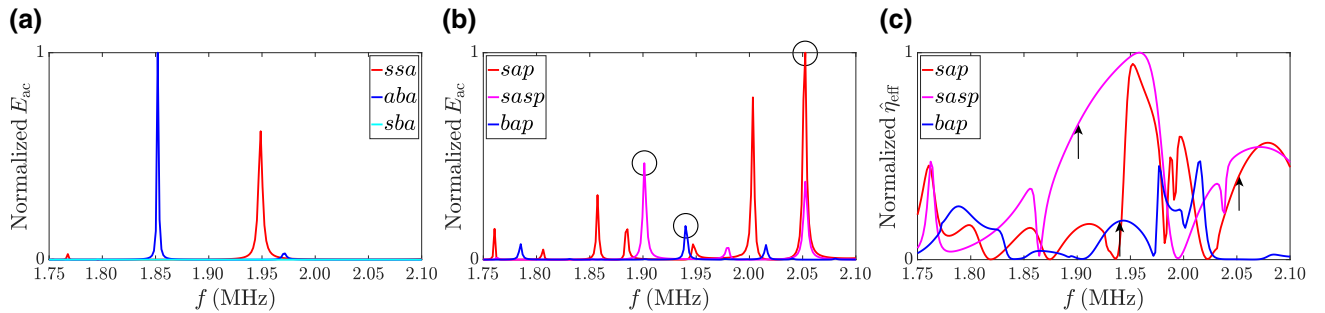


FIG. 11. The E_{ac} value in the frequency range from 1.75 to 2.1 MHz obtained (a) using the ideal models *sba*, *aba*, and *ssa*, and (b) using the models including PZT transducers *bap*, *sap*, and *sasp*. The black circles in (b) indicate the frequencies under which the vibration modes are shown in Figs. 10(d)–10(f). (c) The dimensionless efficiency parameter $\hat{\eta}_{eff}$ in the same frequency range as in (a) and (b) obtained using *bap*, *sap*, and *sasp*. The black arrows in (c) point to the resonance frequencies using *bap*, *sap*, and *sasp*, as indicated by the black circles in (b).

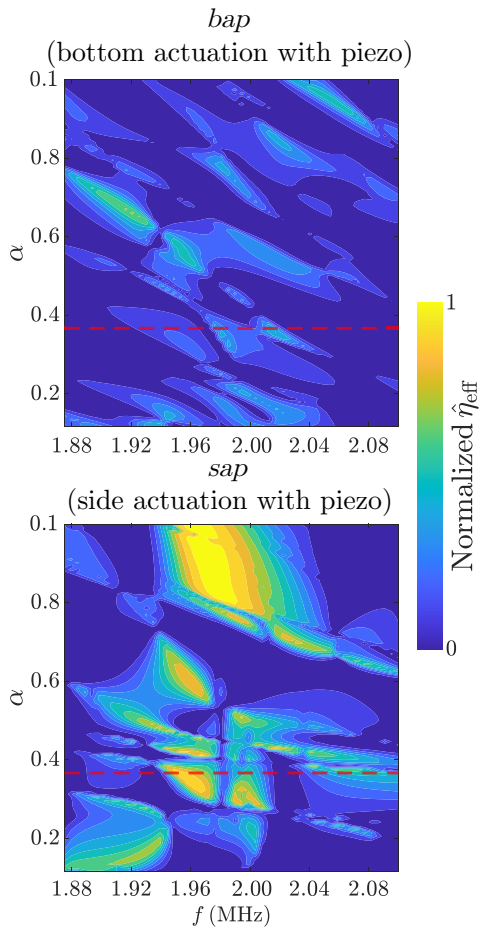


FIG. 12. A parametric study of the efficiency parameter $\hat{\eta}_{\text{eff}}$ at a wide range of the chip aspect ratio α ($0.12 < \alpha < 1$) obtained using *bap* and *sap*. The red dashed lines indicate the α used in experiments ($\alpha = 0.37$).

same conclusion [36]. The results clearly show that side actuation in general leads to a higher energy-conversion efficiency compared to bottom actuation at α values of experimental relevance and that this is not an experimental coincidence that only occurs at the α value of the acoustophoresis devices used in this study.

C. Submicrometer particle focusing

When inhomogeneous fluids are infused to the channel with a higher acoustic impedance medium in the center, the induced acoustic body force stabilizes the fluid configuration against gravity [50]. In addition, this stable configuration leads to the suppression of acoustic streaming, owing to the competition between the boundary-induced streaming stress and the inhomogeneity-induced acoustic body force [17,18]. The focusing of submicrometer particles, which is normally prevented by acoustic streaming, therefore becomes possible with an inhomogeneous medium and the major challenge is the minute radiation force

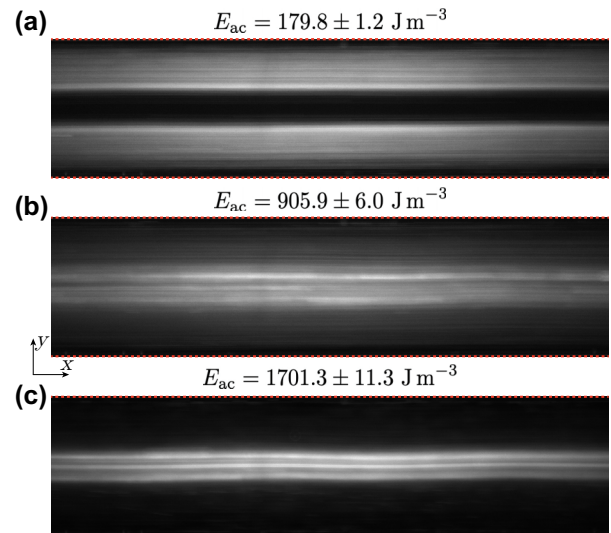


FIG. 13. The focusing of the 500-nm-diameter polystyrene particles under $E_{\text{ac}} =$ (a) 179.8 ± 1.2 , (b) 905.9 ± 6.0 , and (c) $1701.3 \pm 11.3 \text{ J m}^{-3}$, respectively, with a total flow rate of $30 \mu\text{l min}^{-1}$ ($13 \mu\text{l min}^{-1}$ for the side stream and $17 \mu\text{l min}^{-1}$ for the center stream). The flow direction is from the left to the right. The images are taken in front of the trifurcation of the channel outlets. The E_{ac} values are estimated based on the linear dependence of E_{ac} on P_{in} . The channel sidewalls are indicated by the red dashed lines.

acting on the particles due to their small size. Our previous study, using the *bap* configuration, has demonstrated the focusing of particles below the critical size (about $2 \mu\text{m}$ in diameter under the present experimental conditions), but has failed to focus submicrometer particles under a total flow rate of $28 \mu\text{l min}^{-1}$ ($12 \mu\text{l min}^{-1}$ for the side stream and $16 \mu\text{l min}^{-1}$ for the center stream) due to the weak radiation force, even though a power amplifier was used [55].

Here, we perform a similar focusing experiment for 500-nm-diameter particles using a chip actuated from the side with a small PZT transducer. The energy density E_{ac} of the device under each input power P_{in} is estimated based on the linear dependence of E_{ac} on P_{in} . The total flow rate is chosen to be $30 \mu\text{l min}^{-1}$ ($13 \mu\text{l min}^{-1}$ for the side stream and $17 \mu\text{l min}^{-1}$ for the center stream); hence the experimental conditions are comparable to those of our previous study [55]. Very few 500-nm particles are focused to the center stream under a low E_{ac} (around 180 J m^{-3}), as shown in Fig. 13(a), though this level of E_{ac} is far from sufficient to stabilize the liquid configuration to prevent the sedimentation of the dense liquid in the center stream. When E_{ac} is increased to 900 J m^{-3} , a considerable number of 500-nm particles reach the center stream [Fig. 13(b)]. E_{ac} is able to reach more than 1700 J m^{-3} at $P_{\text{in}} = 235 \text{ mW}$ (the highest P_{in} that this device can reach when only driven

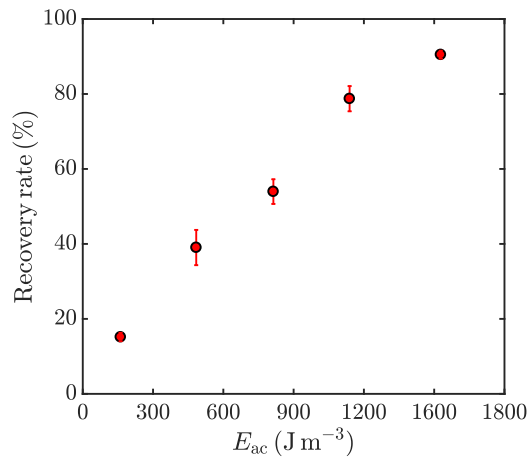


FIG. 14. The recovery rate of the 500-nm-diameter polystyrene particles, which is calculated as the ratio of the number of particles collected from the center outlet to the total number of particles collected from both outlets, measured under $P_{in} = 25, 75, 125, 175,$ and 235 mW, respectively. The E_{ac} value under each P_{in} is estimated based on the linear dependence of E_{ac} on P_{in} .

by a function generator), under which most of the particles are focused to the center stream [Fig. 13(c)]. After counting the numbers of particles in each outlet, it is found that more than 90% of the 500-nm particles are collected from the center outlet, as shown in Fig. 14, which is a significant improvement compared to our previous study, where less than 20% of the 500-nm particles were focused at a similar flow rate. More importantly, the high recovery rate achieved in this study is obtained without using a power amplifier, which clearly demonstrates the advantage of acoustophoresis devices possessing a high energy-conversion efficiency. The high performance of submicrometer particle focusing (high total and sample input flow rates, a high recovery rate, and a low input power) shows clear superiority to that achieved in other acoustofluidic devices using different approaches [55–58].

V. CONCLUSIONS

In this work, we experimentally and numerically demonstrate that side actuation is able to enhance the acoustic energy density and the energy-conversion efficiency in bulk-wave-acoustophoresis devices. Stronger acoustic fields are achieved using side actuation compared to bottom actuation at different input powers indicated by the qualitative free-flow measurements and the acoustic energy density is increased by a factor of 4 using side actuation with a small PZT transducer measured by the confocal micro-PIV. The simulation results are in good agreement with the experimental data and clearly illustrate how the significant symmetry breaking induced by side actuation leads to a stronger sound field

in the microchannel. The numerically conducted parametric study also proves that side actuation produces a higher energy-conversion efficiency with different device aspect ratios. The enhancement in energy-conversion efficiency using side actuation not only applies to the bowl-shaped channel cross section experimentally investigated in this work but also to the rectangular channel cross section, as proven by numerical simulations. We further perform the focusing of 500-nm-diameter particles in inhomogeneous fluids using the device actuated from the side and a recovery rate higher than 90% is achieved at a total flow rate of $30 \mu l \text{ min}^{-1}$ without using a power amplifier. In addition to more efficient driving of acoustophoresis devices compared to conventional bottom actuation, side actuation also provides full optical visibility to the microchannel, which is required in a few specific applications. This study demonstrates the importance of efficient device driving by exciting ideal vibration modes and further improvement can be expected by optimizing the design of piezoelectric transducers and chip geometries.

ACKNOWLEDGMENTS

We appreciate the initial trial of this idea performed by Lei Jiang, when she was a visiting Ph.D. student at Lund University, supported by the China Scholarship Council (CSC) (NO.201806280170). The work was supported by the Swedish Research Council (Grants No. 2018-03672 and No. 2019-00795). W.Q. was supported by the Marie Skłodowska-Curie Actions (MSCA) European Fellowship Seal of Excellence IF-2018 from Vinnova, Sweden’s Innovation Agency (Grant No. 2019-04856) and the grant for scientific research from The Crafoord Foundation (Grant No. 20211029). The spinning-disk confocal microscope used in this study was acquired by funding from the European Research Council (ERC) under the European Union’s Horizon 2020 research and innovation programme (Grant Agreement No. 852590).

- [1] F. Petersson, L. Åberg, A. M. Swärd-Nilsson, and T. Laurell, Free flow acoustophoresis: Microfluidic-based mode of particle and cell separation, *Anal. Chem.* **79**, 5117 (2007).
- [2] P. Augustsson, C. Magnusson, M. Nordin, H. Lilja, and T. Laurell, Microfluidic, label-free enrichment of prostate cancer cells in blood based on acoustophoresis, *Anal. Chem.* **84**, 7954 (2012).
- [3] X. Ding, Z. Peng, S.-C. S. Lin, M. Geri, S. Li, P. Li, Y. Chen, M. Dao, S. Suresh, and T. J. Huang, Cell separation using tilted-angle standing surface acoustic waves, *PNAS* **111**, 12992 (2014).
- [4] C. Grenvall, C. Magnusson, H. Lilja, and T. Laurell, Concurrent isolation of lymphocytes and granulocytes using prefocused free flow acoustophoresis, *Anal. Chem.* **87**, 5596 (2015).

- [5] O. Manneberg, J. Svennebring, H. M. Hertz, and M. Wiklund, Wedge transducer design for two-dimensional ultrasonic manipulation in a microfluidic chip, *J. Micromech. Microeng.* **18**, 095025 (2008).
- [6] X. Ding, S.-C. S. Lin, B. Kiraly, H. Yue, S. Li, I.-K. Chiang, J. Shi, S. J. Benkovic, and T. J. Huang, On-chip manipulation of single microparticles, cells, and organisms using surface acoustic waves, *PNAS* **109**, 11105 (2012).
- [7] D. J. Collins, B. Morahan, J. Garcia-Bustos, C. Doerig, M. Plebanski, and A. Neild, Two-dimensional single-cell patterning with one cell per well driven by surface acoustic waves, *Nat. Commun.* **6**, 8686 (2015).
- [8] B. W. Drinkwater, Dynamic-field devices for the ultrasonic manipulation of microparticles, *Lab Chip* **16**, 2360 (2016).
- [9] M. Evander and J. Nilsson, Acoustofluidics 20: Applications in acoustic trapping, *Lab Chip* **12**, 4667 (2012).
- [10] K. Yasuda, S. S. Haupt, S.-i. Umemura, T. Yagi, M. Nishida, and Y. Shibata, Using acoustic radiation force as a concentration method for erythrocytes, *J. Acoust. Soc. Am.* **102**, 642 (1997).
- [11] M. Nordin and T. Laurell, Two-hundredfold volume concentration of dilute cell and particle suspensions using chip integrated multistage acoustophoresis, *Lab Chip* **12**, 4610 (2012).
- [12] D. Carugo, T. Octon, W. Messaoudi, A. L. Fisher, M. Carboni, N. R. Harris, M. Hill, and P. Glynne-Jones, A thin-reflector microfluidic resonator for continuous-flow concentration of microorganisms: A new approach to water quality analysis using acoustofluidics, *Lab Chip* **14**, 3830 (2014).
- [13] M. Antfolk, C. Magnusson, P. Augustsson, H. Lilja, and T. Laurell, Acoustofluidic, label-free separation and simultaneous concentration of rare tumor cells from white blood cells, *Anal. Chem.* **87**, 9322 (2015).
- [14] P. Augustsson and T. Laurell, Acoustofluidics 11: Affinity specific extraction and sample decomplexing using continuous flow acoustophoresis, *Lab Chip* **12**, 1742 (2012).
- [15] T. Laurell, A. Lenshof, eds., *Microscale Acoustofluidics* (Royal Society of Chemistry, Cambridge, 2015).
- [16] AcouSort AB, www.acousort.com.
- [17] J. T. Karlsen, W. Qiu, P. Augustsson, and H. Bruus, Acoustic Streaming and its Suppression in Inhomogeneous Fluids, *Phys. Rev. Lett.* **120**, 054501 (2018).
- [18] W. Qiu, J. T. Karlsen, H. Bruus, and P. Augustsson, Experimental Characterization of Acoustic Streaming in Gradients of Density and Compressibility, *Phys. Rev. Appl.* **11**, 024018 (2019).
- [19] J. S. Bach and H. Bruus, Suppression of Acoustic Streaming in Shape-Optimized Channels, *Phys. Rev. Lett.* **124**, 214501 (2020).
- [20] K. Yosioka and Y. Kawasima, Acoustic radiation pressure on a compressible sphere, *Acustica* **5**, 167 (1955).
- [21] L. P. Gorkov, On the forces acting on a small particle in an acoustical field in an ideal fluid, *Sov. Phys.—Dokl.* **6**, 773 (1962).
- [22] M. Baudoin, J.-L. Thomas, R. Al Sahely, J.-C. Gerbedoen, Z. Gong, A. Sivery, O. B. Matar, N. Smagin, P. Favreau, and A. Vlandas, Spatially selective manipulation of cells with single-beam acoustical tweezers, *Nat. Commun.* **11**, 4244 (2020).
- [23] P. Sehgal and B. J. Kirby, Separation of 300 and 100 nm particles in Fabry-Perot acoustofluidic resonators, *Anal. Chem.* **89**, 12192 (2017).
- [24] M. Bora and M. Shusteff, Efficient coupling of acoustic modes in microfluidic channel devices, *Lab Chip* **15**, 3192 (2015).
- [25] A. Tahmasebipour, L. Friedrich, M. Begley, H. Bruus, and C. Meinhart, Toward optimal acoustophoretic microparticle manipulation by exploiting asymmetry, *J. Acoust. Soc. Am.* **148**, 359 (2020).
- [26] T. Ikeda, *Fundamentals of Piezoelectricity* (Oxford Science Publications, Oxford, 1996).
- [27] J. J. Hawkes and W. T. Coakley, Force field particle filter, combining ultrasound standing waves and laminar flow, *Sens. Actuator B Chem.* **75**, 213 (2001).
- [28] P. Glynne-Jones, R. J. Boltryk, and M. Hill, Acoustofluidics 9: Modelling and applications of planar resonant devices for acoustic particle manipulation, *Lab Chip* **12**, 1417 (2012).
- [29] J. D. Adams, C. L. Ebbesen, R. Barnkob, A. H. J. Yang, H. T. Soh, and H. Bruus, High-throughput, temperature-controlled microchannel acoustophoresis device made with rapid prototyping, *J. Micromech. Microeng.* **22**, 075017 (2012).
- [30] Y. Gu, C. Chen, Z. Wang, P.-H. Huang, H. Fu, L. Wang, M. Wu, Y. Chen, T. Gao, J. Gong, J. K. Kwun, G. M. Arepally, and T. J. Huang, Plastic-based acoustofluidic devices for high-throughput, biocompatible platelet separation, *Lab Chip* **19**, 394 (2019).
- [31] K. Yasuda, S. Umemura, and K. Takeda, Concentration and fractionation of small particles in liquid by ultrasound, *Jpn. J. Appl. Phys.* **34**, 2715 (1995).
- [32] A. Nilsson, F. Petersson, H. Jönsson, and T. Laurell, Acoustic control of suspended particles in micro fluidic chips, *Lab Chip* **4**, 131 (2004).
- [33] I. Leibacher, P. Reichert, and J. Dual, Microfluidic droplet handling by bulk acoustic wave (BAW) acoustophoresis, *Lab Chip* **15**, 2896 (2015).
- [34] A. Fornell, J. Nilsson, L. Jonsson, P. K. Periyannan Rajeswari, H. N. Joensson, and M. Tenje, Controlled lateral positioning of microparticles inside droplets using acoustophoresis, *Anal. Chem.* **87**, 10521 (2015).
- [35] S. Karthick, P. Pradeep, P. Kanchana, and A. Sen, Acoustic impedance-based size-independent isolation of circulating tumour cells from blood using acoustophoresis, *Lab Chip* **18**, 3802 (2018).
- [36] See the Supplemental Material at <http://link.aps.org/supplemental/10.1103/PhysRevApplied.17.044043> for details about the driving conditions for all nine chips tested in the free-flow focusing experiments using different actuation methods, a photograph of the actual devices, the simulation results for the devices with rectangular channel cross sections, and animations of the vibration modes simulated with bowl-shaped and rectangular channel cross sections.
- [37] M. W. H. Ley and H. Bruus, Continuum modeling of hydrodynamic particle-particle interactions in microfluidic high-concentration suspensions, *Lab Chip* **16**, 1178 (2016).
- [38] R. Barnkob, P. Augustsson, T. Laurell, and H. Bruus, Acoustic radiation- and streaming-induced microparticle velocities determined by microparticle image velocimetry

- in an ultrasound symmetry plane, *Phys. Rev. E* **86**, 056307 (2012).
- [39] P. B. Muller, R. Barnkob, M. J. H. Jensen, and H. Bruus, A numerical study of microparticle acoustophoresis driven by acoustic radiation forces and streaming-induced drag forces, *Lab Chip* **12**, 4617 (2012).
- [40] W. Qiu, H. Bruus, and P. Augustsson, Particle-size-dependent acoustophoretic motion and depletion of micro- and nano-particles at long timescales, *Phys. Rev. E* **102**, 013108 (2020).
- [41] V. Vitali, G. Core, F. Garofalo, T. Laurell, and A. Lenshof, Differential impedance spectra analysis reveals optimal actuation frequency in bulk mode acoustophoresis, *Sci. Rep.* **9**, 19081 (2019).
- [42] M. Settnes and H. Bruus, Forces acting on a small particle in an acoustical field in a viscous fluid, *Phys. Rev. E* **85**, 016327 (2012).
- [43] T. Baasch, I. Leibacher, and J. Dual, Multibody dynamics in acoustophoresis, *J. Acoust. Soc. Am.* **141**, 1664 (2017).
- [44] H. Faxén, The resistance against the movement of a rigid sphere in viscous fluids, which is embedded between two parallel layered barriers, *Ann. Phys.* **68**, 89 (1922).
- [45] J. Happel and H. Brenner, *Low Reynolds Number Hydrodynamics with Special Applications to Particulate Media* (Martinus Nijhoff Publishers, The Hague, 1983).
- [46] M. Koklu, A. C. Sabuncu, and A. Beskok, Acoustophoresis in shallow microchannels, *J. Colloid Interface Sci.* **351**, 407 (2010).
- [47] T. Baasch and J. Dual, Acoustic Radiation Force on a Spherical Fluid or Solid Elastic Particle Placed Close to a Fluid or Solid Elastic Half-Space, *Phys. Rev. Appl.* **14**, 024052 (2020).
- [48] P. Augustsson, R. Barnkob, S. T. Wereley, H. Bruus, and T. Laurell, Automated and temperature-controlled micro-PIV measurements enabling long-term-stable microchannel acoustophoresis characterization, *Lab Chip* **11**, 4152 (2011).
- [49] W. Thielicke and E. Stamhuis, PIVlab—towards user-friendly, affordable and accurate digital particle image velocimetry in MATLAB, *J. Open Res. Softw.* **2**, e30 (2014).
- [50] J. T. Karlsen, P. Augustsson, and H. Bruus, Acoustic Force Density Acting on Inhomogeneous Fluids in Acoustic Fields, *Phys. Rev. Lett.* **117**, 114504 (2016).
- [51] COMSOL MULTIPHYSICS 5.5, www.comsol.com.
- [52] Ferroperm Piezoceramics, www.meggitterferroperm.com.
- [53] A. R. Selfridge, Approximate material properties in isotropic materials, *IEEE Trans. Sonics Ultrason.* **32**, 381 (1985).
- [54] J. S. Bach and H. Bruus, Bulk-driven acoustic streaming at resonance in closed microcavities, *Phys. Rev. E* **100**, 023104 (2019).
- [55] D. Van Assche, E. Reithuber, W. Qiu, T. Laurell, B. Henriques-Normark, P. Mellroth, P. Ohlsson, and P. Augustsson, Gradient acoustic focusing of sub-micron particles for separation of bacteria from blood lysate, *Sci. Rep.* **10**, 3670 (2020).
- [56] M. Antfolk, P. B. Muller, P. Augustsson, H. Bruus, and T. Laurell, Focusing of sub-micrometer particles and bacteria enabled by two-dimensional acoustophoresis, *Lab Chip* **14**, 2791 (2014).
- [57] M. Ugawa, H. Lee, T. Baasch, M. Lee, S. Kim, O. Jeong, Y.-H. Choi, D. Sohn, T. Laurell, S. Ota, and S. Lee, Reduced acoustic resonator dimensions improve focusing efficiency of bacteria and submicron particles, *Analyst* **147**, 274 (2022).
- [58] C. Devendran, K. Choi, J. Han, Y. Ai, A. Neild, and D. J. Collins, Diffraction-based acoustic manipulation in microchannels enables continuous particle and bacteria focusing, *Lab Chip* **20**, 2674 (2020).